Robustness of SAR Sea Ice Type Classification Across Incidence Angles and Seasons at L-Band

Suman Singha, *Member, IEEE*, A. Malin Johansson, *Member, IEEE*, and Anthony P. Doulgeris, *Senior Member, IEEE*

***Abstract*— In recent years, space-borne synthetic aperture radar (SAR) polarimetry has become a valuable tool for sea ice type retrieval. L-band SAR has proven to be sensitive toward deformed sea ice and is complementary compared with operationally used C-band SAR for sea ice type classification during the early and advanced melt seasons. Here, we employ an artificial neural network (ANN)-based sea ice type classification algorithm on a comprehensive data set of ALOS-2 PALSAR-2 fully polarimetric images acquired with a range of incidence angles and during different environmental conditions. The variability within the data set means that it is ideal for making a novel assessment of the robustness of the sea ice classification, investigating the intraclass variability, the seasonal variations, and the incidence angle effect on the sea ice classification results. The images coincide with two different Arctic campaigns in 2015: the Norwegian Young Sea Ice Cruise 2015 (N-ICE2015) and the Polarstern's (PS92) Transitions in the Arctic Seasonal Sea Ice Zone (TRANSSIZ). We find that it is essential to take into account seasonality and intraclass variability when establishing training data for machine learning-based algorithms though moderate differences in incidence angle are possible to accommodate by the classifier during the dry and cold winter season. We also conclude that the incidence angle dependence of backscatter for a given ice type is consistent for different Arctic regions.**

***Index Terms*— Artificial neural network (ANN), L-band, operational service, polarimetry, sea ice, synthetic aperture radar (SAR).**

I. Introduction

IN THIS study, we perform sea ice type classification on a set of L-band synthetic aperture radar (SAR) images acquired during the freezing and early melt season north of Svalbard. Our aim is to study how the incidence angle and the seasonal variation affect the proposed sea ice type classification, as well as the robustness of the algorithm itself (see [1] and [2]). For this, we utilize fully polarimetric ALOS-2 PALSAR-2 images acquired from April 2015 to June 2015. Temperature records from two temporally and spatially overlapping sea ice observations' campaigns, the Norwegian Young Sea Ice Cruise 2015 (N-ICE2015) and Polarstern's (PS92) Transitions in the Arctic Seasonal Sea Ice Zone (TRANSSIZ), show a temperature range from -25 °C to $+2$ °C during the time of satellite image acquisitions. Moreover, the satellite images were acquired with a range of incidence angles. Such a combination of temperature and angles allows us to explore how the sea ice type classification is affected by the incidence angle and the variability with the season.

Due to their ability to penetrate clouds and operate without daylight, SAR images are operationally used to monitor the sea ice in both the Arctic and the Antarctic regions. Detection and monitoring of safe passages are important for shipping in ice infested waters. This includes identification of open water (OW) and thinner sea ice areas that enable energy-efficient passage and the identification of deformed sea ice areas, such as ridges that will impede progress, resulting in higher fuel cost. Multiple studies have shown that L-band SAR can: 1) provide improved contrast between different sea ice types [3]–[10], such as detection and separation of deformed sea ice from the surrounding sea ice [3], [5]–[8]; 2) provide easier separation between first-year ice (FYI) and multiyear ice (MYI) in the early and advanced melt season [5]; and 3) improve separation between second-year ice (SYI) and MYI in the dry ice winter season [9]. Thin ice areas were found in [10] to be easier to detect in the ALOS PALSAR (L-band) than in ASAR (C-band) images when the HH-channel was used, and Aldenhoff *et al.* [11] found that ALOS-2 PALSAR-2 HH/HV data were preferred in identifying thin ice and calm water areas within the ice pack compared with Sentinel-1 images. Frost flowers on top of thin ice were found to be a major contributor to misclassification in HH C-band SAR between thin and thicker sea ice [3]. L-band SAR appears to be less sensitive to small scale roughness (e.g., frost flowers), and a similar misclassification was not observed in the L-band images.

SAR images have a near to far range intensity decay rate, also known as the incidence angle dependence effect, and this effect varies with different sea ice types, e.g., [12]–[21]. This effect is also apparent in L-band SAR though specific

Manuscript received December 11, 2019; revised June 2, 2020 and September 15, 2020; accepted October 22, 2020. This work was supported in part by the Echtzeitdienste für die Maritime Sicherheit II/III (EMS-II/III) Project funded by the Federal Ministry of Education and Research (BMBF), Germany, in part by the Center for Integrated Remote Sensing and Forecasting for Arctic Operations (CIRFA) Norwegian Research Council (NFR) under Project 237906, and in part by the Fram Centre Arctic Ocean Flagship Program via the Automised Large-scale Sea Ice Mapping Project. The work of A. Malin Johansson was supported by the NFR Project Oil spill and newly formed sea ice detection, characterization, and mapping in the Barents Sea using remote sensing by SAR (OIBSAR) under Project 280616. *(Suman Singha and A. Malin Johansson contributed equally to this work.) (Corresponding authors: Suman Singha; A. Malin Johansson.)*

Suman Singha is with Maritime Safety and Security Laboratory, Remote Sensing Technology Institute (IMF), German Aerospace Center (DLR), 28359 Bremen, Germany, and also with the Department of Geography, University of Calgary, Calgary, AB T2N 1N4, Canada (e-mail: suman.singha@dlr.de).

A. Malin Johansson and Anthony P. Doulgeris are with the Department of Physics and Technology, UiT The Arctic University of Norway, 9037 Tromsø, Norway (e-mail: malin.johansson@uit.no).

Color versions of one or more of the figures in this article are available online at https://ieeexplore.ieee.org.

Digital Object Identifier 10.1109/TGRS.2020.3035029

values regarding the slope are less frequent in the literature. Incidence angle dependence for different polarimetric parameters for different sea ice types in the L-band SAR over the Sea of Okhotsk was investigated in [22], and recently, the incidence angle dependence in L-band SAR for FYI and MYI using ALOS PALSAR images in the Canadian Arctic was investigated [23]. In the latter study, images with incidence angles ranging from 18° to 43.3° were used. The incidence angle range used in our study is slightly smaller though the maximum possible range in incidence angles onboard ALOS-2 PALSAR-2 for fully polarimetric data is used.

The easier detection of the deformed sea ice areas and the improved separation of FYI and MYI combined with a recently increased length of the melt season [24], [25] means that L-band SAR is a useful complement to the ongoing C-band SAR missions. L-band SAR was first operationally used onboard a satellite with the launch of Seasat in 1978, followed by the Japan Earth Resources Satellite (JERS-1) in 1992, ALOS PALSAR in 2006, and ALOS-2 PALSAR-2 in 2014, and further new missions are planned, including recently launched SAOCOM-1A (launched in 2018), SAOCOM-1B (2020), ALOS-4 PALSAR-3 (2020), NASA-ISRO's NISAR (2021), and ESA's ROSE-L. The German Aerospace Center (DLR) is also planning an innovative digital beamforming wide-swath twin L-band SAR, TanDEM-L, with a major focus on cryosphere observation. The continued availability of L-band SAR for operational exploitation is, therefore, foreseen.

In this work, we want to evaluate the suitability of L-band sensors with regard to near-real-time (NRT) operational services in ice infested water and explore the two major challenges: effects of incidence angle and seasonal variation. For this, we use ALOS-2 PALSAR-2 images, where the specifics for the images are presented in Section II together with the environmental conditions. The artificial neural network (ANN) and the training and validation data set used are presented in Section III. Results are presented in Section IV, and a discussion is carried out in Section V with final conclusions presented in Section VI.

II. Data Set

A. Study Area

The study area is located in the Arctic Ocean north of Svalbard, between 80 °N–84 °N and 8 °W–25 °E. L-band SAR satellite images were acquired to overlap with the N-ICE2015 sea ice drift campaign in spring and early summer of 2015 [26] and PS92 TRANSSIZ in early summer 2015 [27].

During the N-ICE2015 campaign, R/V Lance was anchored to, and drifted with, four different sea ice floes: Floes 1–4 [26]. R/V Lance was anchored to Floe 3 from April 18 to June 5, 2015, and Floe 4 from June 7 to June 22, 2015. Floe 4 was located within the marginal ice zone, while Floe 3 at the start of the drift was located approximately 200 km into the pack ice. For the PS92 TRANSSIZ campaign, R/V *Polarstern* was used as a base for sea ice *in situ* observations and airborne campaigns, from May 19 to June 28, 2015 [27].

The sea ice within the study areas was primarily a mixture of FYI and SYI [28] though the areas of thinner sea ice types, such as nilas, young gray ice, and young white ice, were observed. The presence of frost flowers was observed on the young ice (YI) during the entire N-ICE2015 drift study (P. Itkin, personal communication).

In Fig. 1, air temperatures measured during the N-ICE2015 campaign are presented. Two different sensors were used to record the air temperature: one situated on the sea ice 300–400 m away from R/V Lance at 2-m a.s.l. [29] and one at 24-m a.s.l. onboard R/V Lance. For details about the temperature recordings, see [30] and [29]. There was a break in the N-ICE2015 drift study from March 19 to April 18, and no weather data were recorded during this time period. Given the consistent seasonal temperatures below −10 °C before and after the break, and until mid-May, we hypothesize that the temperatures were equally low between March 19 and April 18.

In [31] and [32], the year is divided into seasons, where winter is defined as when the air temperatures are below −5°C and the snow cover is dry. This means that scenes acquired before May 15 are considered to be winter scenes (see Fig. 1 and Table I). The air temperatures approached 0 °C thereafter, and the scenes between May 15 and June 7 are considered to be taken during the early melt season. It should be noted that some of the scenes between May 15 and June 1 were collected when temperatures were below −5 °C though the snow cover can no longer be considered to be dry due to a wet recent history. Out of the five different incidence angles, three were acquired during the winter season (light blue rows in Table I), and two of them during the early melt season (red rows in Table I), thereby ensuring that approximately half of the satellite images were acquired during the winter season and the other half during the early melt season.

B. Fully Polarimetric L-Band SAR

The satellite data set was acquired with JAXA's L-band (ALOS-2) PALSAR-2 sensor in the high-sensitive quad polarimetry (HBQ) acquisition mode. The images have a nominal slant range resolution of 5.1 m and an azimuth resolution of 4.3 m. The footprints are 42 km in the range direction and 70 km in the azimuth direction. The data set consists of satellite data with five different mean incidence angles (see Table I). The different incidence angles were preset in the Basic Observation Scenario by JAXA [33], and each average incidence angle corresponds to fixed datum intervals. Each acquisition consists of one to six frames, where each frame corresponds to the nominal acquisition length in the azimuth direction. In total, 108 satellite images are used in this study, and out of these, 102 images are approximately equally distributed for the incidence angles of beams FP6-3, FP6-4, FP6-5, and PF6-7 (see Table I), and the remaining six images are taken with beam FP6-6. It should be noted that, for the temperatures above −10 °C, beams FP6-3 and FP6-7 were available corresponding to an incidence angle separation of approximately 11°.

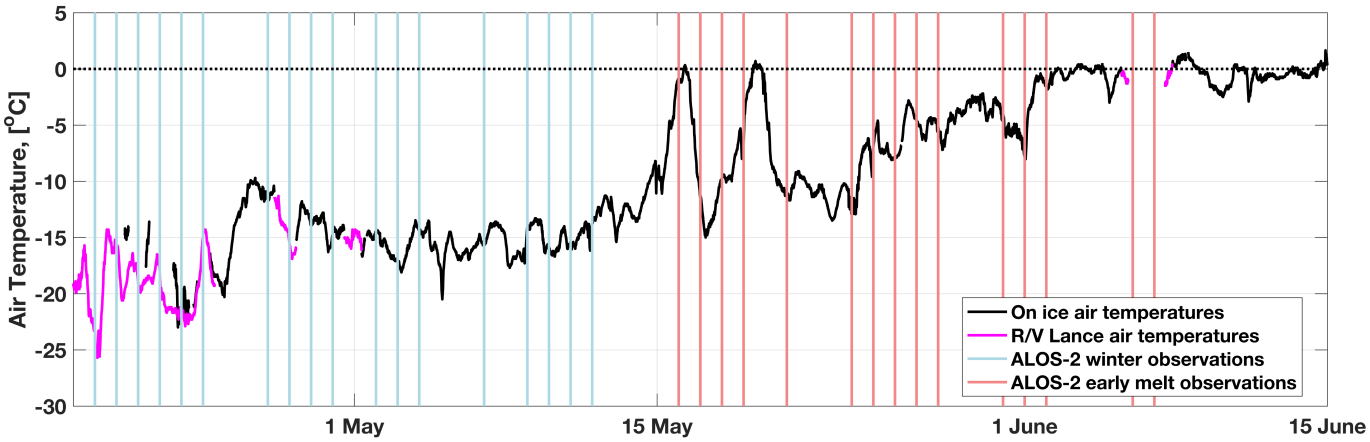

Fig. 1. Air temperature from April 18 to June 15, 2015. The black lines indicate air temperatures measured on the sea ice and the magenta lines the temperatures measured onboard R/V Lance. The black dotted lines indicate 0 °C. Vertical lines indicate the time of the different ALOS-2 PALSAR-2 acquisitions, Blue refers to winter acquisitions, and coral refers to early melt acquisitions.

TABLE I

SENSOR PROPERTIES OF THE ALOS-2 PALSAR-2 IMAGES AND ENVIRONMENTAL CONDITIONS. THE IMAGES ARE HIGH-SENSITIVE QUAD (HBQ) POLARIMETRIC IMAGES. THE ROWS HIGHLIGHTED IN LIGHT BLUE ARE WINTER SCENES, AND THE ROWS HIGHLIGHTED IN CORAL ARE EARLY MELT SEASON SCENES. INCIDENCE ANGLE CORRESPONDS TO THE SCENE CENTER, AND THE TEMPERATURE IS GIVEN AS MEAN ± STANDARD DEVIATION °C

Datum	# images	Incidence Angle, ^{o}	Beam	Temp °C
2015/03/30–2015/04/12	6	36.55	FP6-6	-
2015/04/13–2015/04/26	31	33.91	FP6-5	-17.38±3.08
2015/04/27–2015/05/10	24	31.14	FP6-4	-15.10±1.53
2015/05/11–2015/05/24	24	27.83	FP6-3	-9.64±4.22
2015/05/25–2015/06/07	23	39.05	FP6-7	-3.36±2.47

On March 28, 2017, JAXA released new calibration and validation data for the ALOS-2 PALSAR-2 (from here on ALOS-2) images [34]. This includes updated calibration factors for all satellite imaging modes and an adjusted phase difference between the VV and HH bands for the HBQ modes. The latter change was only applicable for the fully polarimetric stripmap 6-m data on processing level 1.1. For the beams FP6-4 and FP6-6, this meant a phase change of 23.4° and 22.0°, respectively. Further information about the update in the radiometric and polarimetric calibration can be found in [34]. All the images used in this study have been processed with the updated radiometric and polarimetric calibrations. This corresponds to improved signal-to-noise (SNR) ratio in all polarimetric channels. The noise equivalent sigma zero (NESZ) is provided by JAXA as fixed values: one for the two copolarization channels (−36.0 dB) and one for the HV-channel (−46.0 dB) [35].

C. Airborne Measurements

Airborne electromagnetic (AEM) soundings [36] were carried out both as a part of the N-ICE2015 and the PS92 TRANSSIZ campaigns. In this study, we make use of four of those flights to help to identify suitable training and validation areas within the satellite images (see Fig. 2). Three of the flights were from the N-ICE2015 campaign and one

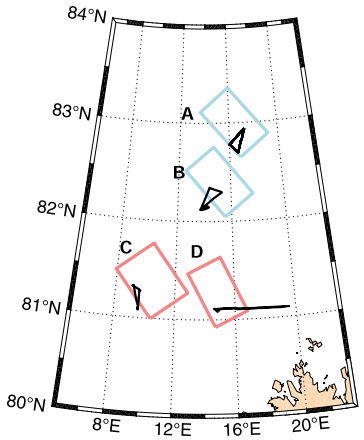

Fig. 2. Overview of the spatially and temporally overlapping ALOS-2 images (light blue rectangles indicating winter scenes and coral rectangles indicating early melt season scenes) and the AEM flights after drift correction (solid black lines).

TABLE II

AEM FLIGHTS USED IN THIS STUDY. FOR EACH OF THE FLIGHTS, THE START TIME AND STOP TIME IN UTC AND THE OVERLAPPING *In Situ* DATA CAMPAIGN ARE PRESENTED. ROW COLOR CODING CORRESPONDS TO WINTER (LIGHT BLUE) AND EARLY MELT SEASON (CORAL). THE # CORRESPONDS TO THE LETTERS USED IN FIG. 2

#	Date	Start time (UTC)	Stop time (UTC)	Campaign	Flight Length
A	24 April	14:24	15:27	N-ICE2015	64.6 km
B	29 April	09:04	10:11	N-ICE2015	95.9 km
C	18 May	11:41	12:22	N-ICE2015	65.8 km
D	8 June	08:16	09:34	PS92 TRANSSIZ	154.5 km

from the PS92 TRANSSIZ campaign (see Table II) in order to assist the selection of the training data set. The AEM flights took place during the day, and the L-band scenes were acquired between 19 and 23 UTC; hence, the AEM flight had to be drift corrected. Assuming that R/V Lance drifted with the same speed and drift pattern as the mean sea ice drift for the area, we used the drift record from R/V Lance, sampled every second, to drift correct the AEM data. Rotational patterns in the sea ice drift were observed by [37] and [38]; hence,

a manual adjustment to the drift correction was also performed. For this manual adjustment, photographs taken during the airborne data collection were used to deduce visual information about the sea ice surface. Furthermore, information and photographs from the AEM flights from the N-ICE2015 campaign can be found in [37], [39], and [40]. Temporally and spatially overlapping airborne laser scanner (ALS) derived freeboard measurements were further used to identify training areas where possible (for further details, see [2]).

III. Methodology

Our aim here is to measure the effect on the sea ice classification results of two distinct types of variations in the data set: seasonal variation and incidence angle effects. In addition, we highlight another often overlooked variation in the training data sets: intraclass variation. To demonstrate this we use a supervised sea ice classification algorithm, the so-called ANN presented in, e.g., [1], [2], and [41], that has proven to produce high-accuracy sea ice type classification result for a range of different frequencies and spatial resolutions. The numerical variations associated with the seasonality and incidence angle effect are studied by exploring the classification results under different configurations of these factors and measured by the change in classification accuracy. The variation in the numerical values will affect all training-based and machine learning approaches to some degree, and as similar variations in different supervised and machine learning approaches have been observed, we argue that the assessment carried out here is transferable to other machine-learning-based sea ice classification methods though the accuracy numbers presented here are only for the ANN approach. A compact summary of the ANN specifics, including polarimetric features, design, coding, and processing, can be found in the Appendix.

The sea ice classifier outputs four classes: those of OW and nilas, YI, smooth FYI (SFYI), and the rough and deformed first year and multiyear ice (RDI). With YI, we mean newly formed ice and refrozen leads, SFYI refers to relatively level ice with low and uniform backscatter, and RDI indicates ice that has undergone deformation resulting in, e.g., ridges of meter scale, or rubble fields, or old ice, which appears brighter compared with SFYI in the radar backscatter domain. In order to assess the incidence angle effect, the seasonality, and the intraclass variability, a range of different training data sets was needed to train and validate the ANN. For the training and validation, a data set was generated with the help of overlapping AEM, ALS, and high-resolution airborne optical images. The AEM has a thickness accuracy of ± 0.10 m [36], enabling easy separation of YI from surrounding thicker sea ice, though there are limitations in separating YI from OW. For the latter, high-resolution airborne optical imageries and the freeboard measurements from ALS taken during flights were, therefore, proven essential. The anticipated incidence angle dependence for the different sea ice types [12]–[20], [22], [23] meant that we created one data set for each different set of incidence angles to investigate the classification consistency. It is also worth mentioning here that the data set was well balanced, i.e., approximately equal number of pixels for each class. In order to access the stability of the training process and determining the classification accuracy, we randomly split the initial training data patches into two disjoint subsets (training and validation samples). It is important to mention here that, during the training process, we trained the classifier with several randomly selected training data sets and selected the trained network with the highest training accuracy. The processing time was approximately 10–12 min in total for feature extraction and classification for a nominal ALOS-2 scene.

The classification was carried out in three different ways.

- *CASE I:* The classification was performed using training data from the same image, the ideal case.
- *CASE II:* The classification was performed using training data from a different image in the same incidence angle data set, highlighting intraclass variations.
- *CASE III:* The classification was performed using the training data from a different image and a different incidence angle data set to explore incidence angle and seasonal variations.

CASE I enables us to assess the accuracy of the sea ice classifier under ideal conditions, i.e., with the same acquisition parameters and minor temperature variations. CASE II explores the intraclass variations by extracting training data from one image and validating the classification results from another image with the same acquisition parameters and similar environmental conditions, whereas CASE III allows us to assess the effects of incidence angle and seasonally induced radar backscatter variation. The limited acquisitions from the ALOS-2 L-band sensor do not cover all possible combinations of incidence angles and seasons, but we can arrive at reasonable conclusions about both season and incidence angle variations. More explicitly, we have three sets of incidence angles covering the winter season and two sets of incidence angles covering the early melt season (see Table I). Therefore, the full sets of CASE III classification and validation allow us to explore the effect of seasonal variations. In order to further explore the stability of the ANN classification scheme, we investigated the variations of the overall accuracy figures for classifiers trained on 31.13° with respect to all three scenarios.

Once the images were classified, a validation of the accuracy was conducted. For the validation of CASE I, the initial training data patches were randomly split into two mutually exclusive subsets: training data set and validation data set. CASE I has already been shown to have a high accuracy, well over 90% (see Table III) [1], [2]. For CASE II, spatially and temporally overlapping optical Landsat-8 images were used to identify new validation areas within ALOS-2 scenes not used in the initial CASE I training. The CASE II validation enables a numerical assessment of the robustness of the classification accuracy within each of the different groups of incidence angles, where the images were acquired at the same incidence angle but at different geographical locations and dates. The validation of CASE III was done across the full set of available training and validation data from each different incidence angle set. The classifications were evaluated based on the overall accuracy of all four classes.

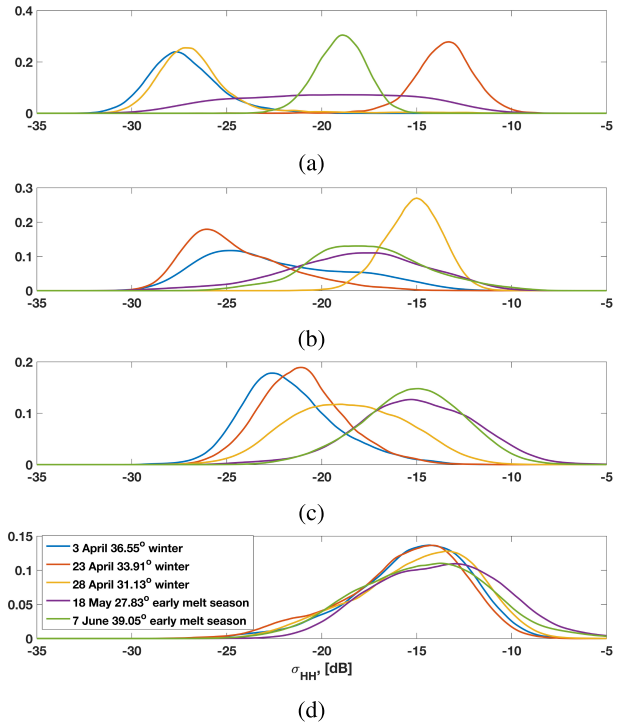

Fig. 3. σ_{HH} pdf's for the different sea ice classes. (a) OW. (b) YI. (c) SFYI. (d) RDI. Each of the different incidence angles is represented by one colored pdf.

IV. Classification Results

The σ_{HH} backscatter values for CASE I are shown in Fig. 3, where the four different sea ice classes [see Fig. 3(a) and (d)] are shown for five different days (in different colors). The OW areas have highly variable backscatter values [see Fig. 3(a)], likely a consequence of varying wind and wave conditions over those areas. The YI areas were also observed to be highly variable in terms of backscatter and reported to be highly correlated with the sea ice thickness and presence of frost flowers [43], [44]. These variations highlight the importance of a training data set spanning a range of different sea states and sea ice thicknesses. Scenes acquired on April 23 were taken shortly after a major storm [38], and with air temperatures below -10 °C, new ice formation was possible, and the YI may, therefore, be very thin. For April 28, the weather conditions had been stable for a few days giving the YI time to stabilize and grow (see [45]). Both the images on April 23 and 28 were acquired in the vicinity of R/V Lance, and some of the observed sea ice was the same within both scenes. The change in thickness for the YI can be observed in the increase in backscatter values occurring between the two scenes. On April 3, overlapping Landsat-8 images show that there are two stages of new ice formation, gray ice, and gray-white ice. These YI formation stages can be observed as the two peaks in the graph [see Fig. 3(b)] with mean values around -25 and -17 dB.

The RDI values overlap under all investigated incidence angles and seasons [see Fig. 3(d)]. The SFYI areas in Fig. 3(c) vary with the different scenes and, consequently, with incidence angle, where a higher incidence angle corresponds to lower backscatter values during the winter season (April 3, April 23, and April 28). During the early melt season (May 18 and June 7), the SFYI values largely overlap each other despite the larger difference in incidence angle, and both the highest and lowest incidence angles here correspond to backscatter values higher than all the winter scenes. Increased backscatter returns at the melt season onset have already been noted in, e.g., [5], [45], and [46]. We attribute this change to physical changes in the snow–sea ice interface, where warmer temperatures likely result in increased brine volume and, hence, increased backscatter values. The melt onset SFYI areas have more homogeneous backscatter values and do not appear to be affected by the 11° incidence angle difference.

We observe that the scene with incidence angle 39.05° does not follow the expected trend of reduced backscatter values with higher incidence angle, but that it closely matches the backscatter values of that acquired during the same season (early melt) but at 27.83° though it should be noted that a higher proportion of those scenes was acquired in the marginal ice zone and resulted in different quantities of sea ice and OW areas. We have also carried out studies on how the different polarimetric features vary with sea ice type, incidence angle, and season, which subsequently affects our classification accuracy using mutual information analysis (see Table V in the Appendix [1], [2]). We observed that the copol power ratio (γ) provides useful and stable information to discriminate OW and different types of sea ice throughout different seasons, but, in terms of discriminating SFYI and RDI, its usefulness is rather limited (see Table IV). On the other hand, geometric intensity (μ), span ($span^{(q)}$, $span^{(d)}$), entropy ($H^{(q)}$, $H^{(d)}$), and α angle ($\alpha^{(q)}$, $\alpha^{(d)}$) provide useful information in terms of discriminating SFYI and RDI. Therefore, a combination of polarimetric features to discriminate different sea ice types and OW is essential to establish a robust classifier.

These combined observations indicate the importance of not only addressing the incidence angle separation but also the seasonality. Due to the lack of a combination of all incidence angles and seasons, it is not possible to fully explore the impact of the season though some initial assessments can be done utilizing the combination of CASE III results (off-diagonal elements in Table III). We observe that the cross-season classification accuracy results presented in Table III are lower than the within season results. For the cross season, higher accuracy is observed when freezing season data are used to classify early melt season images (70%–82%) compared with the opposite.

A. CASE I

The overall classification accuracy for the ideal case, CASE I, can be seen in the second column in Table III. As it can be observed, the overall classification accuracy for CASE I is above 92%. This is in agreement with earlier results reported in [2] and will not be shown further here. In order to demonstrate the robustness of the classifier, we test the variation of the overall accuracy (CASE I) over different images acquired at 33.91°. The average overall accuracy was found to be around 96.1% with a standard deviation of 2.8%.

TABLE III

CLASSIFICATION MATRIX CONTAINING THE COMBINED ACCURACY FOR ALL FOUR CLASSES. THE VERTICAL LINES INDICATE THE INCIDENCE ANGLE THAT THE IMAGES HAVE BEEN TRAINED UPON AND THE HORIZONTAL LINES THE CLASSIFIED IMAGE SETS. THE COLORS IN THE FIRST COLUMN ARE THE SAME AS THOSE USED IN FIG. 3. THE SECOND COLUMN REPRESENTS CASE I, THE GRAY DIAGONAL ELEMENTS REPRESENT CASE II, AND THE OFF-DIAGONAL ELEMENTS BELONG TO CASE III. NOTE THAT THE VARIABILITY FOR CASE I IS CA. 3% WHILE CASE II IS CA. 5% AND CASE III IS CA. 7%–12%

		Images Classified at incidence angle				
ANN Trained on	CASE I	**27.83°**	**31.13°**	**33.91°**	**36.55°**	**39.05°**
27.83°	92.9%	81.5%	68.9%	61.2%	62.5%	68.6%
31.13°	94.9%	70.5%	80.4%	60.2%	61.6%	81.8%
33.91°	96.1% ± 2.8%	70.1% ± 11.8%	72.2% ± 8.2%	83.2% ± 4.8%	83.5% ± 6.8%	69.2% ± 10.3%
36.55°	98.8%	75.8%	74.2%	72.4%	91.0%	80.1%
39.05°	98.6%	79.9%	71.6%	67.4%	68.4%	81.6%

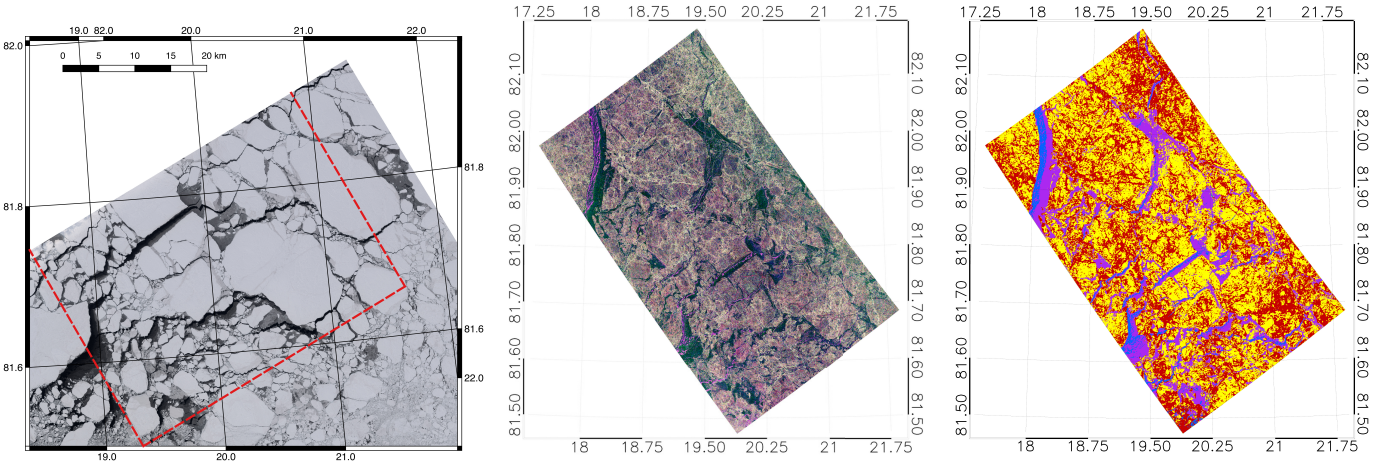

Fig. 4. Satellite images from April 19, 2015. (a) Geocoded RGB composite of Landsat-8. (b) Geocoded Pauli RGB composite of the ALOS-2 acquisition with incidence angle: 33.91°. (c) Classified ALOS-2 image, where blue = OW, purple = YI, yellow = SFYI, and red = RDI. The classification is done using the training data from the same incidence angle though not from the same scene and, thereby, represents CASE II, winter.

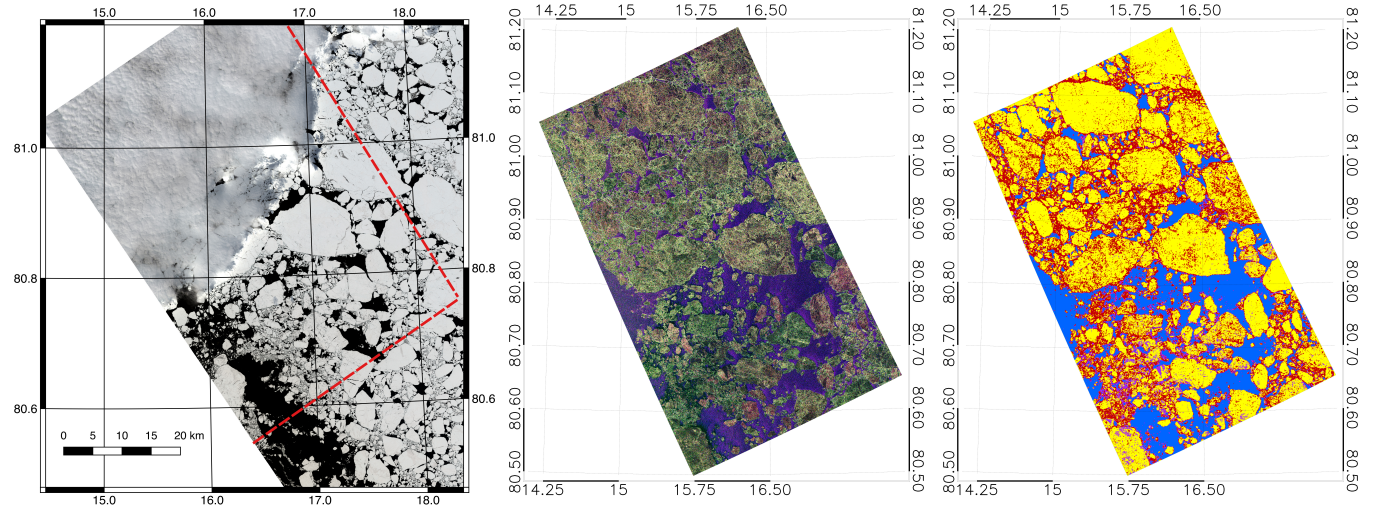

Fig. 5. Satellite images from June 7, 2015. (a) Geocoded RGB composite of Landsat-8. (b) Geocoded Pauli RGB composite of the ALOS-2 acquisition with incidence angle: 39.05°. (c) Classified ALOS-2 image, where blue = OW, purple = YI, yellow = SFYI, and red = RDI. The classification is done using the training data from the same incidence angle though not from the same scene and, thereby, represents CASE II, early melt season.

Furthermore, we assume that the variation would be similar for the other incidence angles.

B. CASE II

Examples of the intraclass variability case, CASE II, can be seen in Figs. 4 and 5, where the ALOS-2 images and classification results are presented with spatially and temporally overlapping Landsat-8 scenes as a reference. As these ALOS-2 images were not used for extracting training ROIs, manual validation of the classification results within each incidence angle group can be performed, and those figures can be treated as a reasonable indicator toward the robustness of

the algorithm. The scenes shown in Fig. 4 were acquired during the winter season, and the scenes in Fig. 5 were acquired during the early melt season. We observe that the sea ice type classification produces satisfactory results when it comes to identifying the OW and the YI areas. Areas classified as SFYI were observed in the Landsat-8 images to correspond to smooth sea ice areas in the classified ALOS-2 image. For the June 7 image, YI areas are not present, and the more extensive OW areas are correctly classified. The Landsat-8 images visually confirm the high percentage of results presented in gray in Table III.

Using overlapping Landsat-8 images, we also observe that an ALOS-2 scene from May 18 is subjected to a flooding of the sea ice. These flooding areas generally have low backscatter values where the deformed sea ice areas are raised above the mean sea ice height and have high backscatter values. These flooded areas are difficult to separate from areas with YI or wet sea ice areas. In addition to flooding, the scenes acquired after May 15 were subjected to changes in the physical structure of the snow cover due to higher temperatures. This can be observed in Fig. 5 where the percentage of SFYI is increasing. To further assess the robustness of the classifier within the same season, we test the variation of the overall accuracy over different images acquired at 33.91°. The average overall accuracy was found to be around 83.2% with a standard deviation of 4.8%.

C. CASE III

The off-diagonals in Table III show the results from CASE III, where the overall accuracy was between 60% and 83.5%. The three mid-range incidence angles (31.13°, 33.91°, and 36.55°) represent satellite images taken during the winter months with dry snow and cold temperatures, highlighted in light blue. The lowest (27.83°) and highest (39.05°) incidence angles investigated within this study were scenes taken during the early melt season, highlighted in coral.

In Fig. 6, classification results for the winter scene on April 23 are shown, where the bottom left shows a CASE I example and the right column is CASE III examples. Overall, the YI and OW areas are correctly identified in all three scenes though the separation between the two shows some differences. The OW and YI areas exhibit potentially large variations in backscatter values highlighting the need for a sufficiently large training data set in order to capture these "intraclass" variations. For the lowest winter incidence angle (trained with 31.13°), the classification contains more SFYI areas than the others, and as can be observed in Table III, the classification accuracy is lower than for the other two winter scenes. This is consistent with the lower overall classification accuracy for this incidence angle group. The results shown in Fig. 6(d) (trained with 36.55°) slightly over-represent the RDI compared with CASE I. It should be noted that larger deformation zones are correctly identified within all three scenes as expected from the probability distributions shown in Fig. 3.

In Fig. 7, the CASE I [see Fig. 7(c)] and CASE III [see Fig. 7(b)] classification results for June 7, 2015, are shown. The OW areas are correctly classified in both images. The brash ice observed between the sea ice floes is classified as RDI in the CASE I classification.

For CASE III, we also test the variation of the overall accuracy over different images (see off-diagonal columns for 33.91°). The standard deviation was found to be around ±6.8%–±8.2% for within season and ±10.3%–±11.8% for across season.

V. Discussion

Within the proposed methodology, we exploited rarely used L-band SAR in an operational context and classified three different sea ice types plus OW using an extensive set of fully polarimetric data. We observe that, for an automatic sea ice type classification, we need to address both the seasonality and the incidence angle influences. First, we will discuss the seasonality and, thereafter, the effect of incidence angles in Sections V-A and V-B.

A. Seasonal Dependence

Seasonal variation directly affects the radar responses from sea ice, especially during the melt seasons as water forms into the upper snow layer of the sea ice resulting in progressively less variable radar backscatter. As extensively described in, e.g., [5], [45], and [47], the backscatter signature changes when the temperatures increases. The temperature effect was most notable in our cross-season CASE III, where the accuracy is higher or similar when the training and validation are kept within the season (see Table III). The largest differences and variations were observed when the early melt season data are used to classify winter scenes. One possible reason for this is the different backscatter signature for SFYI and RDI during the early melt season compared with the winter season (see Fig. 3). However, the seasonal change in the backscatter signature is more pronounced on SFYI compared with RDI.

The 39.05° scene is subjected to wet snow on top, and the difference between deformed ice and smooth ice is somewhat reduced though comparison with Landsat-8 images shows that the major deformation zones are correctly classified (see Fig. 7). The latter is important as it indicates that training data from another season may be used to capture the major obstacles for the shipping industry though the overall sea ice type classification accuracy is reduced.

Although, up until now, only C-band SAR sensors are operationally used, L-band SAR sensors can be exploited effectively for accurate sea ice type classifications in the early melt season (i.e., presence of moist snowpack), which was previously indicated by Onstott [44], while using ground-based scatterometer data, and by Casey *et al.* [5] using SAR data. From this, we conclude that seasonality is important when establishing training data, and especially important is the extraction of training data in the early melt season.

B. Effects of Incidence Angle

The incidence angle effect is explored in our CASE III, where we observe a lower overall classification accuracy for

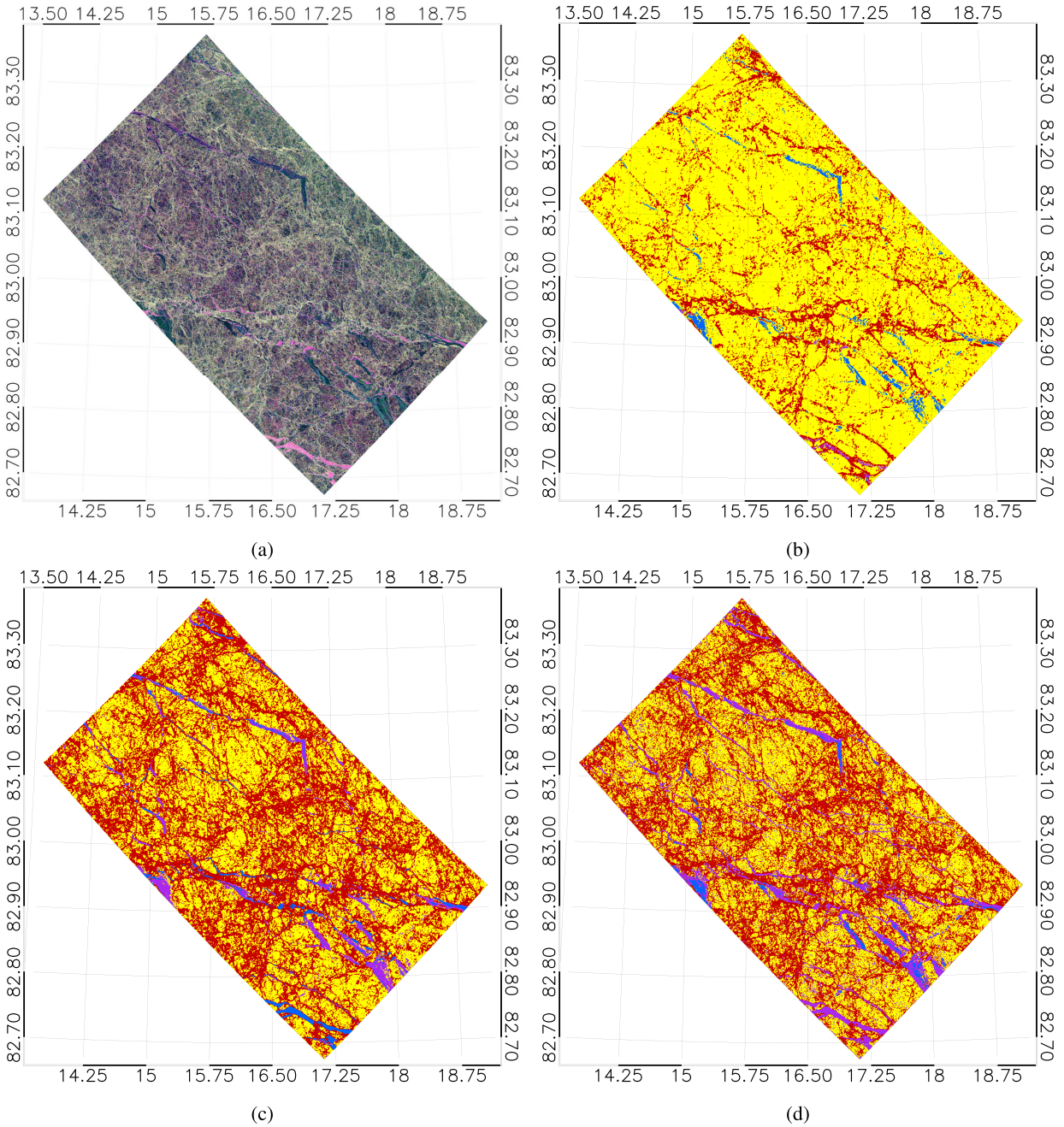

Fig. 6. (a) Geocoded Pauli RGB composite of the ALOS-2 acquisition on April 23, 2015 (incidence angle: 33.91°). Sea ice type classification on ALOS-2 acquisition with ANN trained on (b) 31.13°, (c) 33.91°, and (d) 36.55°. (b) and (d) represent CASE III and (c) represents CASE I, all winter season.

CASE III compared with CASE I and CASE II. This is not surprising as the backscatter values change with incidence angle (see [5], [21]–[23], and [48]) as do the values for other polarimetric features that are used for the classification. In CASE III, during accuracy assessment of each individual image, we observe that the OW and YI areas are correctly separated from SFYI and RDI though they (SFYI and RDI) are in some scenarios misclassified as each other. The major ridges and deformed sea ice are also correctly identified.

From this, we conclude that the incidence angle affects the backscatter (sea ice type) values. However, the different classes are affected differently, and there is sufficient width within the class distribution to allow for some flexibility. This means that we can still produce a usable classification of major sea ice features from adjoining incidence angle ranges of a few degrees under the same season. The incidence angle variation used in this study is limited to a maximum mean difference of 11° (between 27.83° and 39.05°), and the results may, therefore, not be applicable to outside this specific range.

For the three winter scenes, the overall incidence angle dependence for σ_{HH} in this study has a slope of -0.25 and is similar to the slopes observed in [22], [23], and [48] for the winter season using L-band SAR. The average slope for all FYI reported in [23] was -0.21. Similar to earlier studies in, e.g., [14] and [17], Mahmud *et al.* [23] also investigated the difference in slope for different deformation stages, and

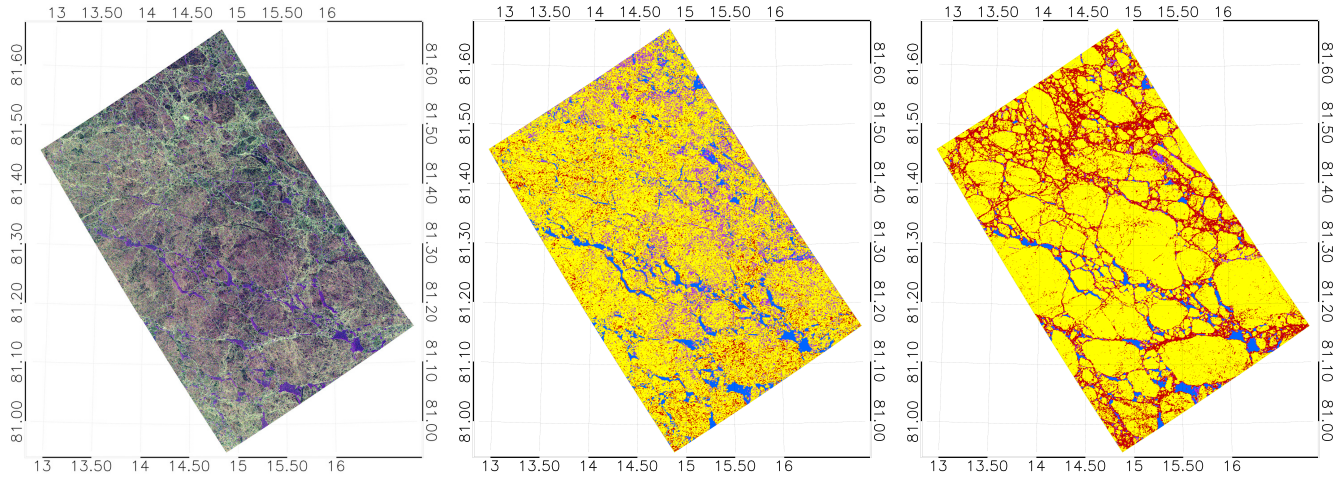

Fig. 7. (a) Geocoded Pauli RGB composite of the ALOS-2 acquisition on June 7, 2015 (incidence angle: 39.05°). Sea ice classification on ALOS-2 acquisition with ANN trained on (b) 27.83° and (c) 39.05°. (b) represents CASE III and (c) CASE I, all early melt season.

the FYI was separated into smooth, deformed, and rough sea ice. It should be noted that we have simply adopted the terminology used in the different studies [5], [22], [23] and have not made an assessment if, e.g., the term rough and smooth corresponds to the same sea ice types in the different studies. Rough FYI in [23] found to have a slope of -0.18, and in [22], a slope of -0.14 was observed. SFYI was estimated to have a slope of -0.23 in [22] and -0.21 in [23].

The winter values reported in [5] show comparable slope and backscatter values to those reported here and in the abovementioned studies. The similarity in the dependence is interesting since the FYI studies include sea ice from the Canadian Arctic Archipelago [5], [23], the area north of Svalbard (this study), and the Sea of Okhotsk [22]. We argue that it may, therefore, be possible to use training data from across the Arctic to train a sea ice type classification neural network, a significant advantage given the cost involved in acquiring *in situ* data. The difference in backscatter values with different incidence angles for the SFYI in the Canadian Arctic Archipelago and the Sea of Okhotsk is 2 dB, and the same difference is observed for the rough FYI (see Fig. 8). Future studies should, therefore, explore the possibility of correcting for systematic feature variation with incidence angle and, thereby, reduce the intraclass variation and ensuring that a coherent training data set can be used to account for a range of incidence angles for winter sea ice type classifications. Moreover, these corrections should be done on a class-by-class basis, including accounting for different FYI types, as our study and those by, e.g., Casey *et al.* [5], Wakabayashi *et al.* [22], and Mahmud *et al.* [23], have found both intraclass and interclass slope variations.

To the best of our knowledge, only a limited number of studies that address the incidence angle effect on early melt season FYI on L-band SAR exist. We observed that the highest incidence angle (39.05°) has values clearly deviating from the otherwise consistent trend with decreasing backscatter values with the incidence angle. This might be due to the fact that rough surfaces are more prominent at higher incidence angles

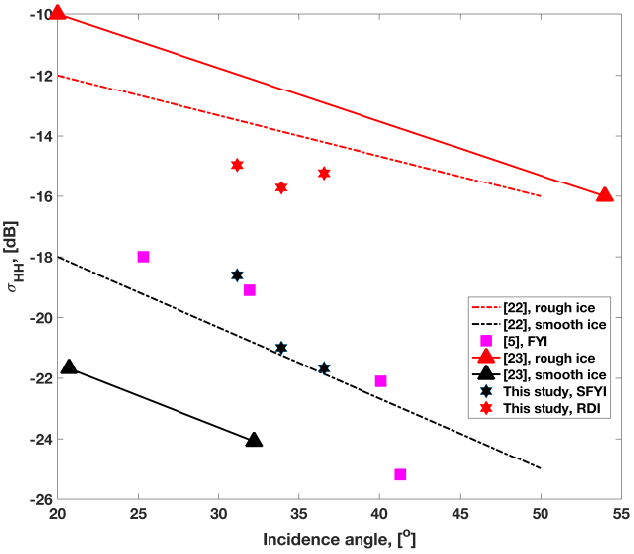

Fig. 8. L-band SAR backscatter coefficient σ_{HH} versus incidence angle for different types of FYI taken from this and previous studies [5], [22], [23].

due to different imaging geometry and different proportions of ice types present in those scenes. In addition, it can be observed in Fig. 3 that the σ_{HH} values for the SFYI and the RDI are largely overlapping in the early melt season despite an incidence angle difference of approximately 11°. In this study, we find that no precise slope can be fit to our early melt season incidence angles, and this appears to also be the case for the values reported in [5]. The adjustment for incidence angle effects may, therefore, be more complex for the melt onset and advanced melt season, and our CASE III results (see Table III) indicate that seasonality may be more important than the incidence angle effect during early melt season and need to be accounted for when training data are established. The interseason maximal standard deviation of overall accuracy was observed (incidence angle: 33.91°) at $\pm 11.8\%$, whereas intraseason maximal standard deviation was observed at $\pm 8.2\%$.

VI. Conclusion

In this work, we conducted thorough investigations on L-band fully polarimetric data set, acquired with different incidence angles and during different seasons, for sea ice type classification into four major categories (OW/Nilas, YI, SFYI, and Rough/Deformed Ice) for an operational environment. One of the major issues, i.e., incidence angle dependencies, has been discussed, and the trend was compared with existing studies that were conducted over different geographic areas along with case-specific classification accuracy assessment for different acquisition and operational scenarios (CASE I, CASE II, and CASE III). The capability of L-band SAR with regard to SFYI and RDI discrimination and better characterization of ridging in sea ice are known for the melt seasons, and these unique qualities of the L-band SAR make it attractive for operational year around usages in the advent of several future L-band SAR missions with wide swath fully polarimetric data (e.g., NISAR, ALOS-4, TanDEM-L, and ROSE-L). Within an operational scenario, given that future L-band SAR missions will provide fully polarimetric data, we recommend that, until a suitable class-by-class correction is developed, the L-band images should be acquired at moderate incidence angle (30°–37°), algorithms should be trained with sufficient intraclass variability, and an independently trained classifier should be used for winter and melt seasons. Furthermore, our results indicate that, for comparable sea ice types, a common incidence angle trend is suitable for three separate areas of the Arctic—the Canadian Arctic Archipelago, the area north of Svalbard, and the Sea of Okhotsk. The observations and findings here are generally valid for machine learning-based algorithms. The status and amount of snow cover on sea ice also play a major role in the robustness of the classifier and are planned to be studied in depth during the ongoing MOSAiC expedition with the help of extensive *in situ* and airborne measurements (https://www.mosaic-expedition.org/).

Appendix

The ANN classifier uses a set of 18 polarimetric features along with its local variances, and the features along with their mathematical definitions are listed in Table IV. Note that, for some features, both dual- and quad-polarimetric versions exist. The dual-polarimetric versions are derived using the two copolarization channels: HH and VV. The features are derived from the well-known coherency matrix T. For the classification algorithm implementation, we used a well-established open-source neural network library in C (FANN) with three hidden layers. The input layer had 36 input neurons and corresponds to 18 polarimetric features and 18 local variances. The first and second hidden layers had 36 hidden neurons each, and the third hidden layer had ten hidden neurons. For the output, we had four output neurons corresponding to each ice type. For further details and earlier implementations of the algorithm, see [1], [2], and [41]. As a part of the standard methodology, the images are radiometrically calibrated using the included metadata information [42], and five × 5-pixel median filters are applied to the data in order to reduce the noise effect before extraction of the polarimetric features.

TABLE IV

Definitions of Polarimetric Features Used in This Study

Quad-polarimetric feature	**Definition**
Entropy, $H^{(q)}$	$H^{(q)} = -\sum_{i=1}^{3} p_i \log_3 p_i$
Anisotropy, $A^{(q)}$	$A^{(q)} = \frac{(\lambda_2^{(q)} - \lambda_3^{(q)})}{(\lambda_2^{(q)} + \lambda_3^{(q)})}$
Mean scattering angle, $\alpha^{(q)}$	$\alpha = \sum_{i=1}^{3} p_i \cos^{-1}(\lvert \boldsymbol{e_i}(1) \rvert)$
Co-pol power ratio, γ	$\gamma = \frac{\langle \lvert S_{HH} \rvert^2 \rangle}{\langle \lvert S_{VV} \rvert^2 \rangle}$
Co-pol phase difference, $\Delta\phi$	$\Delta\phi = \phi_{HH} - \phi_{VV}$
Variance of Co-pol phase difference, $Var(\Delta\phi)$	$Var(\Delta\phi)$
Real part of the copolarization cross product, ρ	$\rho = \lvert \Re\langle S_{HH} S_{VV}^* \rangle \rvert$
Correlation, ε	$\varepsilon = \frac{\langle S_{HH} S_{VV}^* \rangle}{\sqrt{\langle \lvert S_{HH} \rvert^2 \rangle \langle \lvert S_{VV} \rvert^2 \rangle}}$
SPAN, $span^{(q)}$	$span^{(q)} = \text{trace}(T_3)$
Scattering diversity, δ	$\delta = \frac{3}{2}\left(1 - \left(\frac{\lVert T_3 \rVert_F}{span^{(q)}}\right)^2\right)$
Surface scattering fraction, τ	$\tau = \frac{\langle \lvert S_{HH} + S_{VV} \rvert^2 \rangle}{span^{(q)}}$
Geometric Intensity, μ	$\mu = (det(T_3))^{(1/3)}$
Dual-polarimetric feature (HH-VV)	
1st eigenvalue of T_2, $\lambda_1^{(d)}$	
2nd eigenvalue of T_2, $\lambda_2^{(d)}$	
Entropy, $H^{(d)}$	$H^{(d)} = -\sum_{i=1}^{2} p_i \log_2 p_i$
Anisotropy $A^{(d)}$	$A^{(d)} = \frac{(\lambda_1^{(d)} - \lambda_2^{(d)})}{(\lambda_1^{(d)} + \lambda_2^{(d)})}$
Mean scattering angle, $\alpha^{(d)}$	$\alpha = \sum_{i=1}^{2} p_i \cos^{-1}(\lvert \boldsymbol{e_i}(1) \rvert)$
SPAN, $span^{(d)}$	$span^{(d)} = \text{trace}(T_2)$

The eigenvalues of T_3 ($\lambda_1^{(q)}$, $\lambda_2^{(q)}$, $\lambda_3^{(q)}$) and of T_2 ($\lambda_1^{(d)}$, $\lambda_2^{(d)}$) were used to compute $p_i^{(q)} = \lambda_i^{(q)}/(\lambda_1^{(q)} + \lambda_2^{(q)} + \lambda_3^{(q)})$*and* $p_i^{(d)} = \lambda_i^{(d)}/(\lambda_1^{(d)} + \lambda_2^{(d)})$.

TABLE V

Relevance for Distinguishing All Different Classes (All-Class-Relevance). $\mathcal{I}_1$ Denotes $\mathcal{I}(X|\text{Class(all)})/(\mathcal{H}(X))^{1/2}$. Color Coding Corresponds to Winter (Light Blue) and Early Melt Season (Coral)

$\mathcal{I}_1$**(27.83°)**	$\mathcal{I}_1$**(31.13°)**	$\mathcal{I}_1$ **(33.91°)**	$\mathcal{I}_1$**(36.55°)**	$\mathcal{I}_1$**(39.05°)**
γ	μ	μ	γ	γ
μ	$span^{(q)}$	$span^{(q)}$	μ	$\alpha^{(d)}$
$\lambda_2^{(d)}$	$span^{(d)}$	$span^{(d)}$	$span^{(q)}$	$\lambda_2^{(d)}$
$span^{(q)}$	$\lambda_1^{(d)}$	ρ	$span^{(d)}$	δ
$span^{(d)}$	ρ	$\lambda_1^{(d)}$	$\lambda_1^{(d)}$	$H^{(q)}$
ρ	$\lambda_2^{(d)}$	$A^{(d)}$	ρ	$A^{(d)}$
$\lambda_1^{(d)}$	$H^{(q)}$	τ	$\lambda_2^{(d)}$	$H^{(d)}$
$\alpha^{(d)}$	δ	$H^{(d)}$	$\alpha^{(d)}$	μ
$A^{(d)}$	ε	δ	$H^{(q)}$	ε
$H^{(q)}$	τ	$H^{(q)}$	δ	τ
δ	$A^{(d)}$	ε	τ	$\alpha^{(q)}$
$A^{(q)}$	$H^{(d)}$	$\alpha^{(d)}$	$A^{(d)}$	$span^{(q)}$
$H^{(d)}$	$\alpha^{(d)}$	γ	$H^{(d)}$	$A^{(q)}$
ε	γ	$\lambda_2^{(d)}$	ε	ρ
τ	$A^{(q)}$	$A^{(q)}$	$\alpha^{(q)}$	$span^{(d)}$
$\alpha^{(q)}$	$\alpha^{(q)}$	$\alpha^{(q)}$	$A^{(q)}$	$\lambda_1^{(d)}$
$Var\Delta\phi$	$Var\Delta\phi$	$Var\Delta\phi$	$Var\Delta\phi$	$Var\Delta\phi$
$\Delta\phi$	$\Delta\phi$	$\Delta\phi$	$\Delta\phi$	$\Delta\phi$

The processing chain is implanted in the Exelis IDL programming language (image ingestion, calibration, feature extraction, and statistical analysis) and in C (ANN classifier). The hardware specifications that we used were 14-GB RAM, Intel Core i7 3740 QM, and virtual Linux OS.

In Table V, 18 different polarimetric features are ranked with respect to the relevance in terms of the sea ice

classification results, where the data have been separated into the five different incidence angle set. The ranking is based on the overall importance of the distinction between the four different classes (see [1, Sec. IV-A] for further details).

ACKNOWLEDGMENT

This work has been carried out within the framework of DLR-CIRFA(UiT) Scientific Collaboration. The ALOS-2 PALSAR-2 scenes were provided by JAXA under the 4th Research Announcement Program (PI: Torbjørn Eltoft, ALOS PI No. 1199). Landsat-8 images courtesy of the U.S. Geological Survey. The N-ICE2015 expedition was supported by the Centre of Ice, Climate and Ecosystems (ICE), Norwegian Polar Institute, Tromsø, Norway. The authors also extend their thanks to all who participated in the N-ICE2015 campaign, including personnel from the Norwegian Polar Institute, as well as many partner organizations and the R/V Lance crew. They are grateful for the work contributed by those working on PS92 TRANSSIZ and, in particular, Thomas Krumpen (AWI). The views, opinions, and findings contained in this article are those of the authors and should not be constructed as an official DLR position, policy, or decision.

REFERENCES

[1] R. Ressel, S. Singha, S. Lehner, A. Rosel, and G. Spreen, "Investigation into different polarimetric features for sea ice classification using X-band synthetic aperture radar," *IEEE J. Sel. Topics Appl. Earth Observ. Remote Sens.*, vol. 9, no. 7, pp. 3131–3143, Jul. 2016.

[2] S. Singha, A. M. Johansson, N. Hughes, S. M. Hvidegaard, and H. Skourup, "Arctic sea ice characterization using spaceborne fully polarimetric L-, C-, and X-band SAR with validation by airborne measurements," *IEEE Trans. Geosci. Remote Sens.*, vol. 56, no. 7, pp. 3715–3734, Jul. 2018.

[3] W. Dierking and T. Busche, "Sea ice monitoring by L-band SAR: An assessment based on literature and comparisons of JERS-1 and ERS-1 imagery," *IEEE Trans. Geosci. Remote Sens.*, vol. 44, no. 4, pp. 957–970, Apr. 2006.

[4] M. Arkett, D. Flett, R. De Abreu, P. Clemente-Colon, J. Woods, and B. Melchior, "Evaluating ALOS-PALSAR for ice monitoring—What can L-band do for the North American ice service?" in *Proc. IEEE Int. Geosci. Remote Sens. Symp. IGARSS*, Jul. 2008, pp. V-188–V-191.

[5] J. A. Casey, S. E. L. Howell, A. Tivy, and C. Haas, "Separability of sea ice types from wide swath C- and L-band synthetic aperture radar imagery acquired during the melt season," *Remote Sens. Environ.*, vol. 174, pp. 314–328, Mar. 2016. [Online]. Available: http://www.sciencedirect.com/science/article/pii/S003442571530242X

[6] L. E. B. Eriksson *et al.*, "Evaluation of new spaceborne SAR sensors for sea-ice monitoring in the Baltic Sea," *Can. J. Remote Sens.*, vol. 36, p. 56, Jan. 2010.

[7] W. Dierking, "Mapping of different sea ice regimes using images from Sentinel-1 and ALOS synthetic aperture radar," *IEEE Trans. Geosci. Remote Sens.*, vol. 48, no. 3, pp. 1045–1058, Mar. 2010.

[8] W. Dierking and J. Dall, "Sea-ice deformation state from synthetic aperture radar imagery—Part I: Comparison of C- and L-band and different polarization," *IEEE Trans. Geosci. Remote Sens.*, vol. 45, no. 11, pp. 3610–3622, Nov. 2007.

[9] M. Dabboor, B. Montpetit, S. Howell, and C. Haas, "Improving sea ice characterization in dry ice winter conditions using polarimetric parameters from C- and L-band SAR data," *Remote Sens.*, vol. 9, no. 12, p. 1270, Dec. 2017.

[10] W. Dierking, *Thin Ice Classification and Thickness Estimation Using ASAR, PALSAR, RADARSAT-2, and TerraSAR-X Data: First Results*, document ESA SP-686, 2010.

[11] W. Aldenhoff, C. Heuzé, and L. E. B. Eriksson, "Comparison of ice/water classification in Fram Strait from C- and L-band SAR imagery," *Ann. Glaciology*, vol. 59, pp. 112–123, Jul. 2018.

[12] V. H. Kaupp, W. P. Waite, and H. C. Macdonald, "Incidence angle considerations for spacecraft imaging radar," *IEEE Trans. Geosci. Remote Sens.*, vols. GE–20, no. 3, pp. 384–390, Jul. 1982.

[13] J. Karvonen, M. Simila, and M. Mäkynen, "An iterative incidence angle normalization algorithm for sea ice SAR images," in *Proc. IEEE Int. Geosci. Remote Sens. Symp.*, Jun. 2002, pp. 1524–1527.

[14] M. P. Mäkynen, A. T. Manninen, M. H. Simila, J. A. Karvonen, and M. T. Hallikainen, "Incidence angle dependence of the statistical properties of C-band HH-polarization backscattering signatures of the baltic sea ice," *IEEE Trans. Geosci. Remote Sens.*, vol. 40, no. 12, pp. 2593–2605, Dec. 2002.

[15] M. Mäkynen and M. Hallikainen, "Investigation of C- and X-band backscattering signatures of Baltic sea ice," *Int. J. Remote Sens.*, vol. 25, no. 11, pp. 2061–2086, 2004.

[16] D. Isleifson, B. Hwang, D. G. Barber, R. K. Scharien, and L. Shafai, "C-band polarimetric backscattering signatures of newly formed sea ice during fall freeze-up," *IEEE Trans. Geosci. Remote Sens.*, vol. 48, no. 8, pp. 3256–3267, Aug. 2010.

[17] M. Gupta, D. G. Barber, R. K. Scharien, and D. Isleifson, "Detection and classification of surface roughness in an Arctic marginal sea ice zone," *Hydrolog. Processes*, vol. 28, no. 3, pp. 599–609, Jan. 2014.

[18] J. P. S. Gill, J. J. Yackel, T. Geldsetzer, and M. C. Fuller, "Sensitivity of C-band synthetic aperture radar polarimetric parameters to snow thickness over landfast smooth first-year sea ice," *Remote Sens. Environ.*, vol. 166, pp. 34–49, Sep. 2015.

[19] W. Lang, P. Zhang, J. Wu, Y. Shen, and X. Yang, "Incidence angle correction of SAR sea ice data based on locally linear mapping," *IEEE Trans. Geosci. Remote Sens.*, vol. 54, no. 6, pp. 3188–3199, Jun. 2016.

[20] M. Mäkynen and J. Karvonen, "Incidence angle dependence of first-year sea ice backscattering coefficient in Sentinel-1 SAR imagery over the Kara Sea," *IEEE Trans. Geosci. Remote Sens.*, vol. 55, no. 11, pp. 6170–6181, Nov. 2017.

[21] A. S. Komarov and M. Buehner, "Detection of first-year and multi-year sea ice from dual-polarization SAR images under cold conditions," *IEEE Trans. Geosci. Remote Sens.*, vol. 57, no. 11, pp. 9109–9123, Nov. 2019.

[22] H. Wakabayashi, T. Matsuoka, K. Nakamura, and F. Nishio, "Polarimetric characteristics of sea ice in the sea of Okhotsk observed by airborne L-band SAR," *IEEE Trans. Geosci. Remote Sens.*, vol. 42, no. 11, pp. 2412–2425, Nov. 2004.

[23] M. S. Mahmud, T. Geldsetzer, S. E. L. Howell, J. J. Yackel, V. Nandan, and R. K. Scharien, "Incidence angle dependence of HH-polarized C- and L-band wintertime backscatter over Arctic sea ice," *IEEE Trans. Geosci. Remote Sens.*, vol. 56, no. 11, pp. 6686–6698, Nov. 2018.

[24] T. Markus, J. C. Stroeve, and J. Miller, "Recent changes in Arctic sea ice melt onset, freezeup, and melt season length," *J. Geophys. Res.*, vol. 114, no. C12, pp. 1–14, 2009.

[25] J. C. Stroeve, T. Markus, L. Boisvert, J. Miller, and A. Barrett, "Changes in Arctic melt season and implications for sea ice loss," *Geophys. Res. Lett.*, vol. 41, no. 4, pp. 1216–1225, Feb. 2014.

[26] M. A. Granskog, I. Fer, A. Rinke, and H. Steen, "Atmosphere-ice-ocean-ecosystem processes in a thinner Arctic sea ice regime: The Norwegian young sea ICE (N-ICE2015) expedition," *J. Geophys. Res., Oceans*, vol. 123, no. 3, pp. 1586–1594, Mar. 2018. [Online]. Available: https://agupubs.onlinelibrary.wiley.com/doi/abs/10.1002/2017JC013328

[27] P. Ilka. (2016). *The Expedition PS92 of the Research Vessel POLARSTERN to the Arctic Ocean in 2015*. [Online]. Available: http://epic.awi.de/39592/1/BzPM_694_2016.pdf

[28] M. A. Granskog *et al.*, "Snow contribution to first-year and second-year Arctic sea ice mass balance north of Svalbard," *J. Geophys. Res., Oceans*, vol. 122, no. 3, pp. 2539–2549, Mar. 2017, doi: 10.1002/2016JC012398.

[29] S. R. Hudson, L. Cohen, and V. Walden, "N-ICE2015 surface meteorology," Norwegian Polar Inst., Tromsø, Norway, Tech. Rep., 2015, doi: 10.21334/npolar.2015.056a61d1.

[30] L. Cohen, S. R. Hudson, V. P. Walden, R. M. Graham, and M. A. Granskog, "Meteorological conditions in a thinner Arctic sea ice regime from winter to summer during the norwegian young sea ice expedition (N-ICE2015)," *J. Geophys. Res., Atmos.*, vol. 122, no. 14, pp. 7235–7259, Jul. 2017.

[31] C. E. Livingstone, K. P. Singh, and A. L. Gray, "Seasonal and regional variations of active/passive microwave signatures of sea ice," *IEEE Trans. Geosci. Remote Sens.*, vol. GE-25, no. 2, pp. 159–173, Mar. 1987.

[32] D. G. Barber, J. J. Yackel, and J. M. Hanesiak, "Sea ice, RADARSAT-1 and Arctic climate processes: A review and update," *Can. J. Remote Sens.*, vol. 27, no. 1, pp. 51–61, Feb. 2001.

[33] JAXA. (Nov. 2018). *Palsar-2 Basic Observation Scenario Map/User Guideline*. [Online]. Available: https://www.eorc.jaxa.jp/ALOS-2/en/obs/pal2obsguide.htm

[34] T. Motohka, O. Isoguchi, M. Sakashita, and M. Shimada. (2018). *ALOS-2 PALSAR-2 Cal/Val Updates*. [Online]. Available: http://www.eorc.jaxa.jp/ALOS-2/en/calval/JAXA_PI_workshop_ALOS2CalVal_20180124.pdf

[35] M. Shimada, M. Watanabe, T. Motohka, Y. Kankaku, and S. Suzuki, "Calibration and validation of PALSAR-2," in *Proc. IEEE Int. Geosci. Remote Sens. Symp.*, Jul. 2015.

[36] C. Haas, J. Lobach, S. Hendricks, L. Rabenstein, and A. Pfaffling, "Helicopter-borne measurements of sea ice thickness, using a small and lightweight, digital EM system," *J. Appl. Geophys.*, vol. 67, no. 3, pp. 234–241, Mar. 2009.

[37] A. M. Johansson *et al.*, "Combined observations of Arctic sea ice with near-coincident colocated X-band, C-band, and L-band SAR satellite remote sensing and helicopter-borne measurements," *J. Geophys. Res., Oceans*, vol. 122, no. 1, pp. 669–691, Jan. 2017, doi: 10.1002/2016JC012273.

[38] P. Itkin *et al.*, "Thin ice and storms: Sea ice deformation from buoy arrays deployed during N-ICE2015," *J. Geophys. Res., Oceans*, vol. 122, no. 6, pp. 4661–4674, Jun. 2017, doi: 10.1002/2016JC012403.

[39] J. King *et al.*, "Comparison of freeboard retrieval and ice thickness calculation from ALS, ASIRAS, and CryoSat-2 in the Norwegian Arctic to field measurements made during the N-ICE2015 expedition," *J. Geophys. Res., Oceans*, vol. 123, no. 2, pp. 1123–1141, Feb. 2018.

[40] A. M. Johansson, C. Brekke, G. Spreen, and J. A. King, "X-, C-, and L-band SAR signatures of newly formed sea ice in Arctic leads during winter and spring," *Remote Sens. Environ.*, vol. 204, pp. 162–180, Jan. 2018. [Online]. Available: http://www.sciencedirect.com/science/article/pii/S0034425717304960

[41] R. Ressel and S. Singha, "Comparing near coincident space borne C and X band fully polarimetric SAR data for Arctic sea ice classification," *Remote Sens.*, vol. 8, no. 1, p. 57, 2016. [Online]. Available: http://www.mdpi.com/2072-4292/8/3/198

[42] M. Shimada, O. Isoguchi, T. Tadono, and K. Isono, "PALSAR radiometric and geometric calibration," *IEEE Trans. Geosci. Remote Sens.*, vol. 47, no. 12, pp. 3915–3932, Dec. 2009.

[43] D. P. Winebrenner, L. D. Farmer, and I. R. Joughin, "On the response of polarimetric synthetic aperture radar signatures at 24-cm wavelength to sea ice thickness in Arctic leads," *Radio Sci.*, vol. 30, no. 2, pp. 373–402, Mar. 1995, doi: 10.1029/94RS02313.

[44] R. G. Onstott, *SAR Scatterometer Signatures Sea Ice*. Washington, DC, USA: American Geophysical Union, 1992, pp. 73–104, doi: 10.1029/GM068p0073.

[45] H. M. Kauko *et al.*, "Windows in Arctic sea ice: Light transmission and ice algae in a refrozen lead," *J. Geophys. Res., Biogeosci.*, vol. 122, no. 6, pp. 1486–1505, Jun. 2017. [Online]. Available: https://agupubs.onlinelibrary.wiley.com/doi/abs/10.1002/2016JG003626

[46] S. E. L. Howell, D. Small, C. Rohner, M. S. Mahmud, J. J. Yackel, and M. Brady, "Estimating melt onset over arctic sea ice from time series multi-sensor Sentinel-1 and RADARSAT-2 backscatter," *Remote Sens. Environ.*, vol. 229, pp. 48–59, Aug. 2019.

[47] D. G. Barber, T. N. Papakyriakou, E. F. Ledrew, and M. E. Shokr, "An examination of the relation between the spring period evolution of the scattering coefficient (σ) and radiative fluxes over Jandfast sea-ice," *Int. J. Remote Sens.*, vol. 16, no. 17, pp. 3343–3363, Nov. 1995.

[48] T. Geldsetzer, M. Arkett, T. Zagon, F. Charbonneau, J. J. Yackel, and R. K. Scharien, "All-season compact-polarimetry C-band SAR observations of sea ice," *Can. J. Remote Sens.*, vol. 41, no. 5, pp. 485–504, Sep. 2015, doi: 10.1080/07038992.2015.1120661.

[49] J. Karvonen, E. Rinne, H. Sallila, and M. Mäkynen, "On suitability of ALOS-2/PALSAR-2 dual-polarized SAR data for Arctic sea ice parameter estimation," *IEEE Trans. Geosci. Remote Sens.*, vol. 58, no. 11, pp. 7969–7981, Nov. 2020.

Suman Singha (Member, IEEE) received the M.Tech. degree in remote sensing from IIT Roorkee, Roorkee, India, in 2009, and the M.Sc. degree in remote sensing and the Ph.D. degree in microwave remote sensing from the University of Hull, Hull, U.K., in 2010 and 2014, respectively.

He was a Visiting Scientist with the European Maritime Safety Agency (EMSA), Lisbon, Portugal, in 2012. Since 2013, he has been a Research Scientist with the Remote Sensing Technology Institute (IMF), German Aerospace Center (DLR), Bremen, Germany. Since 2020, he has been an Adjunct Assistant Professor with the Department of Geography, University of Calgary, Calgary, AB, Canada. His research interest includes the application of artificial intelligence and machine learning approaches to classify traditional and polarimetric synthetic aperture radar (SAR) images with an emphasis on sea ice properties retrieval and oil spill detection.

A. Malin Johansson (Member, IEEE) received the M.Sc. degree in physical oceanography from Gothenburg University, Gothenburg, Sweden, in 2005, and the Ph.D. degree in remote sensing from Stockholm University, Stockholm, Sweden, in 2012.

She was a Post-Doctoral Researcher with the Radar Remote Sensing Group, Department of Earth and Space Sciences, Chalmers University of Technology, Gothenburg. She joined the Department of Physics and Technology, UiT The Arctic University of Norway, Tromsø, Norway, in 2014, where she is also a Research Scientist. Her research interest includes multisensor remote sensing of sea ice and oil spills.

Anthony P. Doulgeris (Senior Member, IEEE) received the B.Sc. degree in physics from The Australian National University, Canberra, ACT, Australia, in 1988, and the M.Sc. degree and the Ph.D. degree in physics from the Department of Physics and Technology, UiT The Arctic University of Norway, Tromsø, Norway, in 2006 and 2011, respectively.

He joined the Department of Physics and Technology, UiT The Arctic University of Norway, in 2007, where he is also an Associate Professor and the Head of the Earth Observation Group. His research interests focus on developing generic algorithms for remote sensing, pattern recognition, and multidimensional statistical modeling, in particular for polarimetric synthetic aperture radar (SAR) applications in sea ice and glaciers.